Coastal Dynamics 2017
Paper No. 179

LARGE-SCALE EXPERIMENTAL OBSERVATIONS OF WAVE-INDUCED SEDIMENT TRANSPORT OVER A SURF ZONE SANDBAR

Ryan S. Mieras[1], Jack A. Puleo[1], Dylan Anderson[2], Daniel T. Cox[2] and Tian-Jian Hsu[1]

Abstract

A large-scale laboratory experiment was conducted to evaluate cross-shore sediment transport and bed response over a surf zone sandbar under field-scale wave conditions. Observations of intra-wave sediment mass flux, transport rates and net volume of sediment transport on the crest of a sandbar are presented. The ensemble-averaged total volume of sediment transported per wave in the suspended load layer was of the same order of magnitude as the volume transported in the sheet flow layer. The net volume transported via sheet flow was positive (onshore-directed) for all 11 test conditions. In the cases where suspended sediment transport dominated sheet flow, the net transported volume of sediment was always offshore-directed, whereas, when sheet flow dominated suspended sediment transport, the net volume of sediment transport was always onshore-directed.

Key words: suspended sediment transport, sheet flow, surf zone sandbar, large wave flume experiment, cross-shore sediment transport

1. Introduction

The total amount of sediment transported by waves and currents (total load) in the surf zone is traditionally separated into three modes of transport (neglecting wash load): suspended load, bed load and sheet flow. *Suspended load* is the total volume of sediment in suspension, supported by turbulent fluid motions. Although suspended sediment concentrations are relatively small (c_{SS} ~ 1 – 300 g/L) in the surf zone, the suspended load regime spans the majority of the water depth, h. *Bed load* is often characterized by the intermittent saltation and/or rolling of sand grains across the seabed, meaning the bed load layer is only a few grain diameters thick (Nielsen, 1992). The presence of small bed forms (i.e. sand ripples) is an indicator that bed load may be the dominant transport regime, though suspended load can also be present (Traykovski, 2007).

Small-scale bed forms are wiped out with the onset of sheet flow under strong bed shear stresses. *Sheet flow* is the transport of high concentrations of sediment (c_{SF} ~ 300 – 1500 g/L) supported by intergranular interactions within a relatively thin layer near the bed. The thickness of the sheet layer, δ_S, expands and contracts with the passing of each wave, varying from a few millimeters to several centimeters (Dohmen-Janssen and Hanes, 2002; O'Donoghue and Wright, 2004; Ribberink et al., 2008; Van der Zanden, 2016; Mieras et al., in review). While the sheet layer thickness is generally 1 – 3 orders of magnitude smaller than the water depth in the surf zone ($\delta_s \ll h$), average sediment concentrations in the sheet layer are 1 – 3 orders of magnitude greater than those in suspension ($c_{SF} \gg c_{SS}$). Consequently, it is possible that the contribution of sheet load to the total volume of transported sediment is similar in magnitude to the contribution of suspended load.

Most operational coastal morphology models incorrectly assume that total load consists of only suspended load and bed load, with no explicit inclusion of sheet flow (e.g. Bailard, 1981). Bathymetric evolution models are generally calibrated via tunable parameters in the bed and suspended load formulations to maximize skill in predicting the shape of observed beach profiles over time (Gallagher et al., 1998; Hoefel and Elgar, 2003; Fernández-Mora et al., 2015), rather than being calibrated against observations of the physical processes which lead to the changing bathymetry (e.g. suspended load, bed load and sheet flow). As a result, such

1 Center for Applied Coastal Research, University of Delaware, 259 Academy St., Newark, DE, USA, 19716. ryanmieras@gmail.com (corresponding author), jpuleo@udel.edu, thsu@udel.edu

2 Coastal and Ocean Engineering Program, Oregon State University, Corvallis, OR, USA, 97331. dlaw.anderson@gmail.com, dan.cox@oregonstate.edu

models often exhibit poor predictive skill on operational time scales under varying wave and environmental conditions (Plant et al., 2004; Ruessink and Kuriyama, 2008).

2. Laboratory Experiment

The sandbar sediment transport experiment (BARSED) was conducted in 2015 in the large wave flume at Oregon State University's O.H. Hinsdale Wave Research Laboratory (Mieras et al., in review; Anderson et al., in review). A fixed, barred beach profile was constructed to near-field scale, based on an observed beach profile during the Duck94 experiment (Gallagher et al., 1998; Scott et al., 2005). However, in place of a concrete slab, a steel sediment pit was installed on the sandbar crest (Figure 1) and filled with well sorted sand (d_{50} = 0.17 mm, d_{16}= 0.10 mm, d_{84} = 0.26 m). The hybrid beach profile design allowed for the isolation of small-scale bed response to large-scale wave forcing over an immobile sandbar, where an array of sensors was positioned to measure hydrodynamic forcing and sediment response (Figure 2).

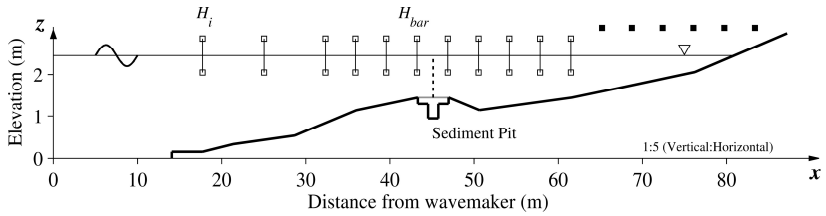

Figure 1. Beach profile and sediment pit, where the vertical dashed line (---) on the sandbar crest indicates the location of the instrument frame in Figure 2a. Surface piercing wave gauges are represented by vertical lines with open squares, and ultrasonic wave gauges are shown as solid squares.

Each trial consisted of 10 periodic waves (1 wave ≡ 1 ensemble) to minimize seiching effects and development of a steady flow component (i.e. undertow). Trials were repeated to obtain a synoptic dataset. The term "wave case" refers to all repeated trials conducted using the same wave maker input signal. Wave heights measured at the seaward toe of the profile (H_i, Figure 1) ranged from 0.38 m to 0.66 m and wave periods (T) from 5.0 s to 9.0 s for the 11 wave cases analyzed in this paper (Table 1). Wave heights measured at the seaward edge of the sandbar crest (H_{bar}, Figure 1) ranged from 0.55 m to 0.94 m.

The velocity profile in the water column (u, v, w ; cross-shore, spanwise, vertical) was measured at 100 Hz with a vertical array of six Nortek Vectrino acoustic Doppler velocimeters (ADV; Figure 2). The lowest ADV (ADV_1) was deployed 0.10 m above the initial bed level with the subsequent ADVs deployed at increments of 0.20 m relative to ADV_1 such that the highest ADV (ADV_6) was 1.10 m above the bed (0.10 m above the still water line). The near-bed velocity profile was measured at 100 Hz with Nortek Vectrino acoustic Doppler profiling velocimeters (ADPV; Figure 2) (Craig et al., 2011). The ADPV resolved 0.03 m of the velocity profile with 0.001 m bin size.

Suspended sediment concentration profiles were measured at 8 Hz using fiber optic backscatter sensors (FOBS; Figure 2) (Beach et al., 1992). The FOBS consisted of a pair of probes, each with 10 optical backscatter sensors, that were deployed vertically offset from each other by 0.09 m. The lowest 2 – 3 sensors were deployed into the sediment bed. The vertical offset between individual sensors on each probe varied from 0.01 m on the lower probe, and 0.02 m to 0.07 m for the higher probe. In total, the FOBS resolved 20 points of suspended sediment concentration within the lower 0.48 m of the water column. Sediment concentration profiles in the sheet layer were measured at 8 Hz with conductivity concentration profilers (CCP; Figure 2) (Lanckriet et al., 2013). The CCPs provided instantaneous 29-point profiles of sediment concentration with 0.001 m vertical measurement spacing. The CCPs were buried in the sediment bed such that the measurement probes (1.6 mm thick x 5.6 mm wide) intersected the sand-water interface (Figure 2b). Adjacent CCPs were offset vertically to expand the vertical range of sheet flow that could be captured under changing bed levels.

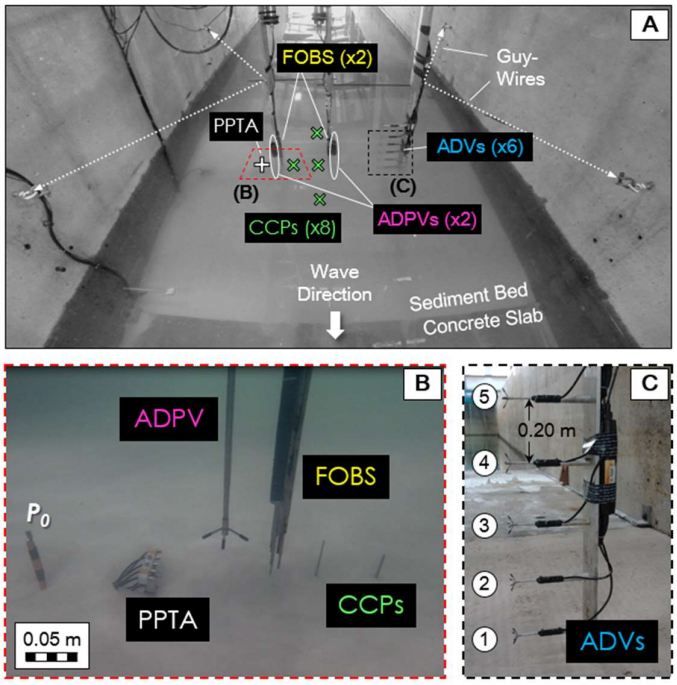

Figure 2. (a) Instrumentation deployed on/over the sandbar, marked by a vertical dashed line in Figure 1. (b) Close-up view of the instrumentation at Site 4, outlined by a dashed red box in (a). The photo was taken prior to the pit being entirely filled with sediment so that the PPTA (Anderson et al., in review) and CCPs would be clearly visible. (c) Close-up view of the lower 5 of 6 ADVs ($ADV_1 - ADV_5$), outlined by the dashed black box in (a).

An underwater view of the near-bed instrumentation is provided in Figure 2b (see Anderson et al., in review for details about the pore-pressure transducer array; PPTA). A mirrored version of the configuration of sensors at Site 4 (ADPV, FOBS and CCPs; Figure 2b) was deployed at the same cross-shore location (~ 0.6 m away from Site 4, in the positive y-direction) (Site 2). A near-bed pressure sensor (P_o; Figure 2b) was used to track the free surface at the same cross-shore location as the other instrumentation. Guy wires were anchored to the flume sidewalls to stabilize the instruments as waves shoaled and broke around the mounting wings. Additional details regarding the BARSED experiment are discussed in Mieras et al. (in review) and Anderson et al. (in review).

Table 1. Summary of wave cases with select wave conditions, where N is the number of ensembles used during phase-averaging for each wave case.

Case ID	T (s)	H_i (m)	H_{bar} (m)	N
S1T5H40	5.0	0.41	0.55	10
S1T5H45	5.0	0.46	0.62	10
S1T5H50	5.0	0.52	0.73	19
S1T5H60	5.0	0.60	0.87	30
S1T7H40	7.0	0.44	0.59	30
S1T7H45	7.0	0.52	0.65	20
S1T7H50	7.0	0.55	0.76	39
S1T7H60	7.0	0.66	0.94	30
S1T9H40	9.0	0.38	0.49	28
S1T9H50	9.0	0.46	0.64	30
S1T9H60	9.0	0.58	0.78	20

3. Data Analysis

The number of repeated trials with useable data (i.e. the bed interface was captured with a CCP at Site 2 or 4) within a given wave case ranged from 1 to 4. An ensemble (n) is composed of a single wave within a trial, so each trial contained 10 potential ensembles. However, four of the trials contained an ensemble with data that was disqualified through quality control and assurance procedures. Therefore, the total number of ensembles, N, for a given wave case ranged from $10 \leq N < 40$ (Table 1). Section 3.1 outlines the procedure that was followed for each trial within a given wave case.

3.1. Data analysis method for a single trial

3.1.1. Merging sediment concentration and velocity profiles

Instantaneous sediment concentration data recorded by the CCP and FOBS were interpolated (linearly) at 100 Hz to match the sampling frequency of the velocity measurements. FOBS data were further interpolated (linearly) to 0.001 m vertical resolution to match the vertical resolution of the CCP. A time series of concentration profiles, $c(t,z)$, from the bed ($z \approx 1.46$ m) to the top of the FOBS ($z \approx 1.92$ m) was constructed by merging the instantaneous profiles measured by the CCP and FOBS at either Site 2 or Site 4 (Figure 3a), depending at which site CCPs captured the immobile bed and sheet layer.

Recirculating flow tank calibrations of the FOBS sensors demonstrated that the signal began to saturate at volumetric sediment concentrations, ϕ, around 0.05 m^3/m^3 ($c \sim 130$ g/L). Moreover, the CCP is less reliable for $\phi < 0.05$ m^3/m^3. Therefore, at each time step, if concentrations were observed by both a FOBS and a CCP at a particular elevation, and $\phi_{CCP} > 0.05$ m^3/m^3, precedence was given to CCP data (Figure 3b). The fact that sediment concentrations observed by the CCP (c_{SF}) and FOBS (c_{SS}) differ by 1 – 3 orders of magnitude (as pointed out in § 1) is shown by the range of mass concentrations, 1 g/L < $c(t,z)$ < 1,000 g/L (Figure 3a).

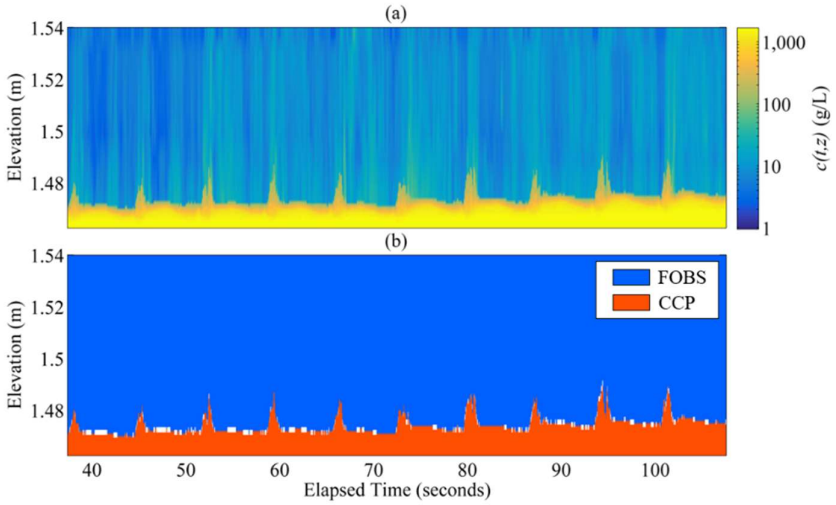

Figure 3. Time-space diagrams of (a) merged, instantaneous sediment mass concentrations in the lower 0.07 – 0.08 m of the water column (S1T7H60: Trial 14, Site 4); (b) mask for the concentration data in (a), denoting where concentrations were derived from CCP measurements (red area), FOBS measurements (blue area), or linearly interpolated (white area).

A time series of the cross-shore velocity profile, $u(t,z)$, from the bed to the elevation of ADV_6 ($z \approx$ 2.55 m) was constructed by merging the instantaneous profiles measured by the ADPV and ADV array. As the waves passed, ADV_5 and ADV_6 were periodically inundated then exposed in air, so the free surface elevation – derived from near-bed pressure measurements (P_0; Figure 2b) – was used to exclude ADV data when the sensors were exposed to air (see Figure 5a). Velocities were approximated between the highest ADPV measurement and the elevation of ADV_1 via linear interpolation.

3.1.2. Separating instantaneous profiles into ensembles

The merged time series of $u(t,z)$ and $c(t,z)$ were separated into ensembles based on zero up-crossings of $P_0(t)$. Sediment mass concentrations were converted to volumetric concentration, ϕ, by dividing by the sediment density, ρ_s (= 2,650 kg/m^3). Each ensemble of velocity $u(t/T,z)_n$ and volumetric concentration $\phi(t/T,z)_n$ were interpolated onto a uniform, normalized time vector with 0.01 second time increments varying between 0 and 1, t/T_n, where T_n is the elapsed time between zero up-crossings for the n^{th} ensemble. The following sub-sections in Section 3 outline the analysis conducted on each ensemble within a trial.

3.1.3. The sheet flow layer and z-coordinate*

The elevation of the top of the sheet layer, $\left[z(t/T)_{top}\right]_n$ (red line; Figure 4b), was defined as the 0.08 m^3/m^3 volumetric concentration contour (Bagnold, 1956). The bottom of the sheet layer, $[z(t/T)_{bott}]_n$ (black line; Figure 4b), was determined by fitting a composite power law and linear curve to each instantaneous concentration profile to identify the sharp shoulder transition in each sheet flow concentration profile (O'Donoghue and Wright, 2004; Lanckriet et al., 2014; Mieras et al., in review). To account for changing bed levels during a trial (see Anderson et al., in review), and different initial and final bed levels for separate trials, data for each ensemble were assigned a 'local' z^*-coordinate, where $z^* = 0$ is the elevation of the inflection point, $\left[z(t/T)_{inf}\right]_n$ (white line; Figure 4b), in the sheet flow concentration profile at each zero up-crossing (see Mieras et al., in review),

$$(z^*)_n = z - \left[z(t/T=0)_{inf}\right]_n . \tag{1}$$

3.1.4. Velocity profile in the sheet flow layer

The high-frequency (10 MHz) underwater acoustic signal emitted from the ADPV is rapidly attenuated in the dense sheet flow layer, so the velocity profile in the sheet layer, $u_{SF}(t/T,z^*)$, was approximated by extrapolating the measured velocity at the top of the sheet layer down to zero velocity at the bottom of the sheet layer (Sumer et al., 1996; Pugh and Wilson, 1999; Wang and Yu, 2007),

$$[u_{SF}(t/T,z^*)]_n = u\big(t/T\,,z^*(t/T)_{top}\big)_n \left(\frac{z^* - z^*(t/T)_{bott}}{z^*(t/T)_{top} - z^*(t/T)_{bott}}\right)_n^{\alpha}, \tag{2}$$

where $u(t/T,z^*(t/T)_{top})$ is the measured velocity at the top of the sheet layer and α is a "profile shape parameter" with $0 < \alpha \leq 1$, $\alpha = 1$ being a linearly decreasing profile. In this paper, α = 0.50 is used (Wang and Yu, 2007; Puleo et al., in revision). Some ensembles had instances in time where the velocity was not measured at the top of the sheet layer due to the bed eroding below the lowest measurement bin of the ADPV (i.e. > 0.07 m below the ADPV transducer). In such instances, the velocity profile in the sheet layer was not approximated. Velocity magnitude of 0 m/s was assigned to bins below the bottom of the sheet layer (Figure 4b-c).

3.2. Data analysis method for each wave case

The subsequent *N* ensembles of velocity, $u(t/T,z^*)_n$, and volumetric sediment concentration, $\phi(t/T,z^*)_n$, were individually interpolated onto a universal grid with vertical grid spacing above the sheet layer of 0.01 m, which was the minimum vertical resolution of FOBS measurements. Horizontal volumetric sediment flux, $(\phi u)_n$, was computed for each ensemble by multiplying $u(t/T,z^*)_n$ and $\phi(t/T,z^*)_n$.

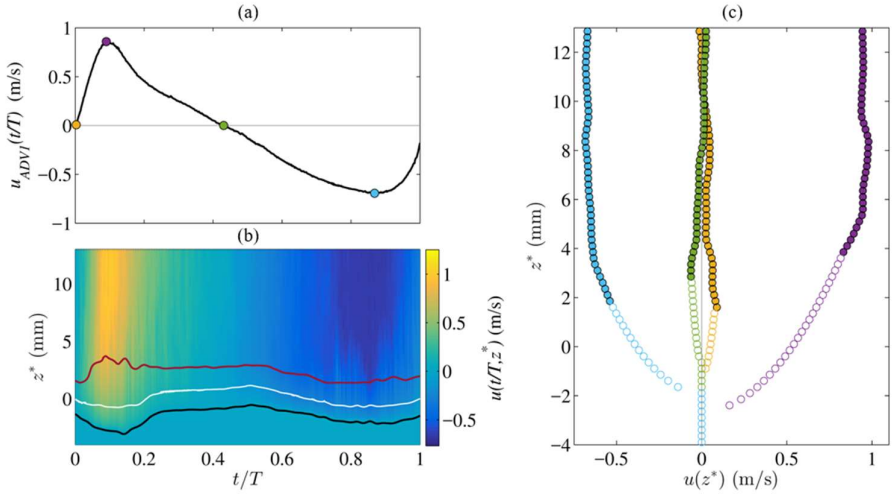

Figure 4. Measured cross-shore velocities and approximated velocities in the sheet layer, for the 3rd ensemble (n = 3) from Trial 18 (S1T7H40, Site 4). (a) Cross-shore velocity measured by ADV_1 (z^* = 0.103 m), where the 4 colored dots correspond to the phases of: offshore to onshore flow reversal (gold), peak crest velocity (purple), onshore to offshore flow reversal (green) and peak trough velocity (light blue). (b) Time-space diagram of cross-shore velocities measured by the ADPV at Site 4 (above red line) and approximated with equation (2) (below red line). The top of the sheet layer ($z^*(t/T)_{top}$; red line), bottom of the sheet layer ($z^*(t/T)_{bott}$; black line), and elevation of the inflection point in each concentration profile ($z^*(t/T)_{inf}$; white line) are also shown. (c) Select cross-shore velocity profiles with the colors and phases corresponding to panel (a). Filled circles (●) are measured data and open circles (○) are approximated using equation (2) and α = 0.50.

3.2.1. Sediment transport rates

The net suspended sediment transport rate for each ensemble, $q_{SS}(t/T)$, in the cross-shore direction was computed using

$$[q_{SS}(t/T)]_n = \rho_s \int_{[z^*(t/T)_{top}]_n}^{[z^*_{FOBS,20}]_n} \phi(t/T\,, z^*)_n u(t/T\,, z^*)_n \, dz^* \;; \quad n = 1 \ldots N, \tag{3}$$

where $z^*_{FOBS,20}$ is the elevation of the highest (20th) FOBS measurement bin (see Figure 5a), which is roughly located at mid-depth. Likewise, net sheet flow sediment transport rate, $q_{SF}(t/T)$, in the cross-shore direction was computed by integrating the horizontal flux over the sheet layer thickness,

$$[q_{SF}(t/T)]_n = \rho_s \int_{[z^*(t/T)_{bott}]_n}^{[z^*(t/T)_{top}]_n} \phi(t/T\,, z^*)_n u(t/T\,, z^*)_n \, dz^* \;; \quad n = 1 \ldots N. \tag{4}$$

3.2.2. Net transported volume

The net volume of sediment transported (per meter flume width, per wave) as suspended load, V_{SS}, and as sheet flow, V_{SF}, for each (n^{th}) ensemble was computed by integrating the sediment transport rate over the wave cycle and multiplying by the wave period (and dividing by sediment density),

$$(V_{SS})_n = \frac{T}{\rho_s} \int_0^1 [q_{SS}(t/T)]_n \, d(t/T) \;; \quad n = 1 \ldots N \tag{5}$$

and

$$(V_{SF})_n = \frac{T}{\rho_s}\int_0^1 [q_{SF}(t/T)]_n \, d(t/T) \; ; \quad n = 1 \ldots N \, . \tag{6}$$

4. Preliminary Results

The intra-wave components of the measured and derived transport quantities were obtained through ensemble averaging, which effectively removes the turbulent components from the signal. Ensemble-averaged quantities were computed as

$$\langle \xi(t/T \, , z^*) \rangle = \frac{1}{N}\sum_{n=1}^{N} \xi\left(\frac{t}{T}, z^*\right)_n \, , \tag{7}$$

where ξ represents either a measured or derived quantity and the angled brackets, $\langle \, \rangle$, denote ensemble averaging.

4.1. *Ensemble-averaged velocity and sediment mass flux*

An example time-space diagram (S1T9H60) of ensemble-averaged cross-shore velocities resolved by the vertical array of 6 ADVs and a near-bed ADPV is given in Figure 5a. As the crest of the wave passes the array, ADV_6, which is 0.10 m above the still water line, becomes inundated and wave velocities are captured within the crest ($t/T \sim 0 - 0.2$; Figure 5a). Ensemble-averaged near-bed velocities (< 0.05 m) captured by the ADPV are given in Figure 5b, along with the ensemble-averages of the approximated velocities in the sheet layer (red/black lines; Figure 5b) via equation (2). The development of the wave bottom boundary layer is evident by the closely spaced contours of increasingly darker shades of blue in the wave trough (Figure 5b).

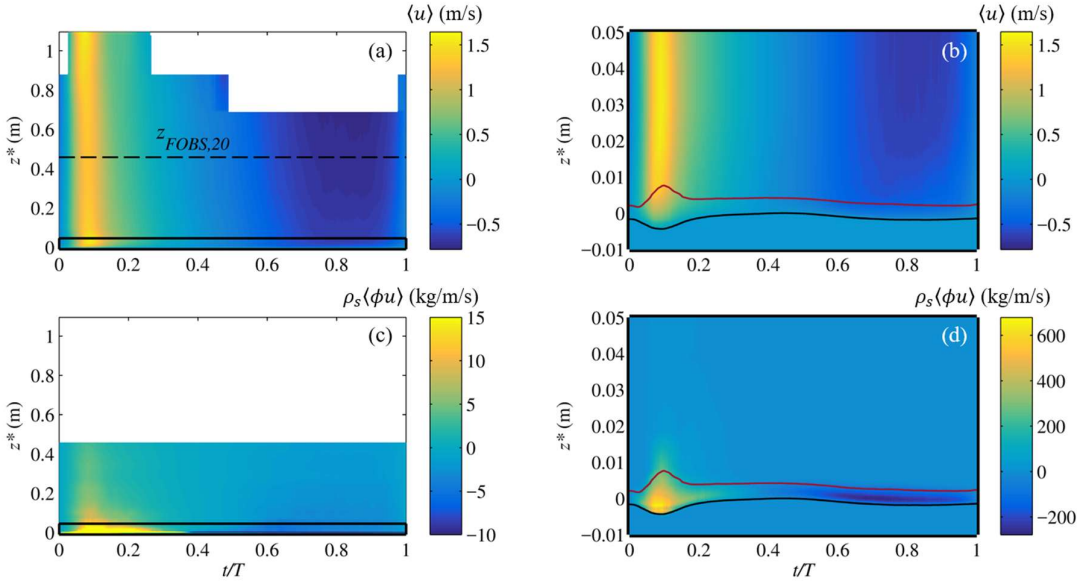

Figure 5. Time-space diagrams of ensemble-averaged cross-shore (a) – (b) velocity, and (c) – (d) sediment mass flux for S1T9H60. The elevation of the 20th FOBS bin, $z^*_{FOBS,20}$ (dashed black line), is marked in (a). The thick black rectangles in (a) and (c) outline the domain of near-bed (< 0.05 m) velocity and mass flux shown in (b) and (d), respectively. In addition, the top (red line) and bottom (black line) of the sheet layer are given in (b) and (d).

Ensemble-averaged horizontal sediment mass flux in the lower half of the water column for case S1T9H60 is provided in Figure 5c, while the near-bed mass flux, and sediment mass flux in the sheet layer, are shown in Figure 5d. However, the range of magnitudes of sediment mass flux between the two vertical regimes differ by up to 40 times (Note the smaller upper and lower limit of the colorbar in Figure 5c compared with those in Figure 5d). Maximum horizontal sediment mass flux in the sheet layer occurs in phase with maximum erosion depth (black line) and is 3 times greater than the maximum mass flux in the wave trough (Figure 5d). But the duration of elevated (negative) values of sediment mass flux within the sheet layer in the trough is 2 – 3 times longer than beneath the wave crest.

4.2. Ensemble-averaged sediment transport rates

Comparisons between the ensemble-averaged net sediment transport rate in the sheet layer, $\langle q_{SF} \rangle$, and suspension layer, $\langle q_{SS} \rangle$, for three different wave cases reveals that both transport rates are of the same order of magnitude (Figure 6). However, the peak transport rates for the longer period waves (S1T7H45 and S1T9H50; Figure 6c,e) are up to twice as much as the peak transport rates for shorter wave period and smaller wave height (S1T5H50; Figure 6a).

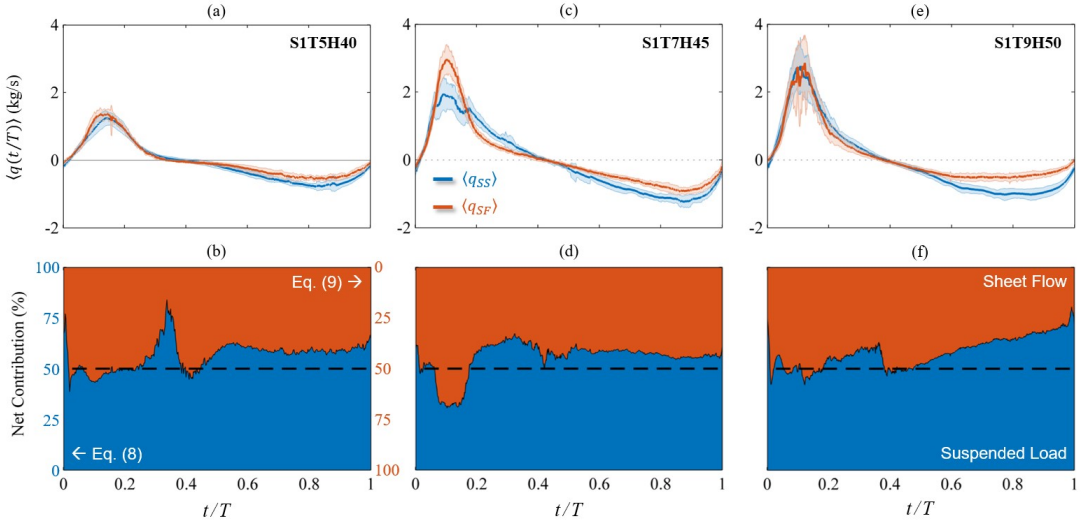

Figure 6. Ensemble-averaged cross-shore sediment transport rates (suspended sediment, $\langle q_{SS} \rangle$, and sheet flow, $\langle q_{SF} \rangle$, components) and the net contribution of each transport component to the overall transport rate as a function of phase (equations (8) and (9)), for three different wave cases: (a) – (b) S1T5H50, (c) – (d) S1T7H45, and (e) – (f) S1T9H50. Red colors represent sheet flow, while blue colors represent suspended sediment transport. The lighter shades of red and blue in (a), (c) and (e) are the standard deviations about the ensemble-average transport rates. The dashed black lines in (b), (d) and (f) represent equal contribution by suspended sediment and sheet flow.

Dual-color area plots are used to visualize which transport mode is more dominant throughout the wave cycle (Figure 6). The net contributions (in percent) of suspended sediment transport and sheet flow to the overall transport rate, as a function of wave phase, are given by the following ratios, respectively:

$$\frac{|\langle q_{SS} \rangle|}{|\langle q_{SF} \rangle + \langle q_{SS} \rangle|} \times 100\,, \tag{8}$$

and

$$\frac{|\langle q_{SF} \rangle|}{|\langle q_{SF} \rangle + \langle q_{SS} \rangle|} \times 100\,. \tag{9}$$

Equal contribution from both suspended sediment transport rate and sheet flow transport rate is marked with

a horizontal black dashed line at 50% (Figure 6b,d,e). When sheet flow is the dominant mode, red colors drop below the dashed line, whereas blue colors rise above the dashed line when suspended load contributes more than 50% to the overall sediment transport rate. Suspended load dominates in the trough region for all three wave cases, and, to a lesser degree, sheet flow dominates under the wave crest (Figure 6). Most notably, the sediment transport rate in the sheet layer accounts for nearly 70% of the total at peak transport rate under the wave crest for wave case S1T7H45 (Figure 6c-d).

While the net contributions as tabulated by equations (8) and (9) provide valuable information as a function of wave phase, the result can be misleading and should be interpreted carefully. For example, during on-offshore flow reversal for S1T5H40 ($t/T \sim 0.37$), the contribution of suspended load suddenly jumps to more than 75% (Figure 6b), suggesting that almost all of the sediment transport occurred in the suspended layer. However, the sediment transport rate at this time is effectively zero (Figure 6a). A similar trend is present for the other two wave cases (Figure 6d,f). Therefore, the preceding analysis of net contribution is supplemented in the next section by also comparing the net contributions of suspended sediment transport and sheet flow over the wave period.

4.3. Ensemble-averaged net transported volume

The ensemble-averaged net volume of sediment transported (per meter flume width, per wave) in either suspension or sheet flow for all 11 wave cases is shown in Figure 7. The majority of the cases (9 of 11) exhibited net suspended sediment transport directed offshore (negative values). Conversely, the net volume of sediment transported as sheet flow was always onshore-directed (positive values). The two cases where the net transported volume was onshore-directed for both suspended transport and sheet flow were S1T7H60 and S1T9H60 (see Figure 5).

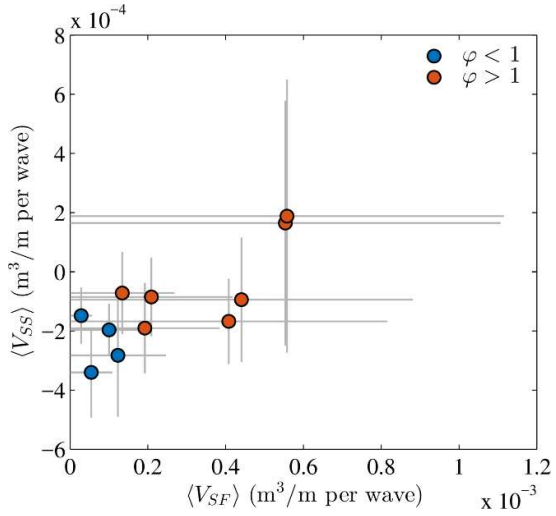

Figure 7. Ensemble-averaged net volume of sediment transported via sheet flow, $\langle V_{SF} \rangle$, and suspended sediment, $\langle V_{SS} \rangle$, per meter flume width, per wave, for the 11 test cases. The grey error bars show one standard deviation from the mean. Negative values signify offshore-directed sediment transport. Marker colors correspond to equation (10).

The ratio of the ensemble-averaged total (absolute value of net) volume of sediment transported as sheet flow to the ensemble-averaged total volume transported in suspension,

$$\varphi = \frac{\langle |V_{SF}| \rangle}{\langle |V_{SS}| \rangle}, \tag{10}$$

highlights two concepts: (i) which mode of transport is more important over the span of one wave, and (ii) how much more dominant one mode of transport is than the other. For $\varphi > 1$, sheet flow is the dominant mode of transport over the wave cycle (i.e. more than 50% of the sediment transport occurred in the sheet

flow layer), while suspended sediment transport is the dominant mode for $\varphi < 1$. The color of the markers in Figure 7 illustrates which mode of transport is dominant (blue ≡ suspended load dominant; red ≡ sheet flow dominant). The magnitude of φ identifies the factor by which one mode of transport dominates the other. For example, $\varphi = 2$ indicates twice as much sediment was transported in the sheet flow layer than was transported in the suspended layer, whereas the opposite is true for $\varphi = 0.5$. The ratio defined by equation (10) for all 11 wave cases is given in Table 2. Visually, $\varphi = 1$ corresponds to equal areas of red and blue in Figure 6 (lower panels), which is essentially the case for S1T7H45 (Figure 6d).

Table 2. Ensemble-averaged net volume of sediment transport as sheet flow and suspended sediment, and the ratio given in equation (10), for each wave case.

Case ID	$\langle V_{SF} \rangle$ (m^3/m per wave)	$\langle V_{SS} \rangle$ (m^3/m per wave)	$\langle V_{SF} \rangle + \langle V_{SS} \rangle$ (m^3/m per wave)	φ
S1T5H40	0.000029	-0.000148	-0.000119	0.19
S1T5H45	0.000055	-0.000340	-0.000285	0.16
S1T5H50	0.000209	-0.000085	0.000124	2.45
S1T5H60	0.000123	-0.000282	-0.000159	0.44
S1T7H40	0.000100	-0.000197	-0.000097	0.51
S1T7H45	0.000192	-0.000190	0.000002	1.01
S1T7H50	0.000408	-0.000168	0.000240	2.43
S1T7H60	0.000554	0.000165	0.000719	3.36
S1T9H40	0.000134	-0.000072	0.000062	1.87
S1T9H50	0.000441	-0.000094	0.000347	4.67
S1T9H60	0.000558	0.000188	0.000746	2.97

The majority of sediment was transported in suspension for 4 of the 11 cases ($\varphi < 1$), whereas sheet flow dominated the total volume of transported sediment in 7 of the 11 cases ($\varphi > 1$); however, one of the cases (S1T7H45) had a φ-value of 1.01, which means sheet flow and suspended sediment transport volumes were essentially equal. For the cases that were dominated by sheet flow, up to nearly 5 times ($\varphi = 4.67$) as much sediment was transported in the sheet layer compared to the volume transported in suspension. Similarly, for the cases dominated by suspended sediment transport, up to 6 times ($\varphi = 0.16$) more sediment volume was transported in suspension compared to the volume transported in the sheet layer.

Both the magnitude and direction (onshore or offshore) of the net volume of sediment transported, $V_{net} = \langle V_{SF} \rangle + \langle V_{SS} \rangle$ (Table 2), correlate well with φ. In general, V_{net} is negative (offshore) when suspended load dominates ($\varphi < 1$), positive (onshore) when sheet flow dominates ($\varphi > 1$), and nearly zero (= 2 x 10^{-6} m^3/m/wave) when $\varphi \sim 1$. The magnitude of V_{net} increased for increasing magnitudes of φ when $\varphi > 1$, while V_{net} became increasingly negative with decreasing values of φ for the cases where $\varphi < 1$.

5. Discussion and Conclusions

Measurements of sheet flow and suspended sediment transport on a large-scale laboratory surf zone sandbar with the application of novel and unique sensors were presented. Observations of intra-wave cross-shore sediment mass flux, sediment transport rates, and net volume of sediment transport revealed that in general, suspended sediment transport was on the same order of magnitude as sheet flow (Figure 6 and Figure 7).

In one case, the volume of sediment transported in suspension was essentially equal to the volume transported as sheet flow (S1T7H45), but with opposite direction, resulting in near-zero net volume of transported sediment. However, if only the suspended load was considered – as may be estimated in a bed-load/suspended-load-based morphological model – the net result would incorrectly imply offshore sediment transport. These findings suggest that (i) for particular wave conditions, sheet flow has an important role in onshore sandbar migration, and (ii) neglecting sheet flow in morphological models will lead to improperly biasing the magnitude and/or direction of suspended sediment transport in order to compensate for excluding sheet flow sediment transport.

Despite elongated troughs (skewed-asymmetric waves) due to waves shoaling over the sandbar, ensemble-averaged net volume of sediment transported in the sheet layer was positive (onshore) for all 11 cases, again highlighting the potential importance of sheet flow in driving onshore sandbar migration. The always-onshore average sheet flow transport volume is likely due to a combination of greater sheet thickness and velocity under the wave crests (positive velocity phase) relative to sheet thickness and velocity under wave troughs (see Mieras et al., in review).

The magnitude of φ given by equation (10) relates the magnitudes of net transported volumes of sediment in both the suspended load layer and the sheet flow layer. The net volume of sediment transported in suspension is a function of the suspension layer thickness, which depends on the elevation of the top of the sheet flow layer and the free-surface elevation. Given the setup for BARSED (Figure 2), suspended sediment concentrations were measured up to ~ 0.5 m above the bed, leaving sediment concentrations in the upper half of the water column up to the free-surface unresolved, which may lead to under-estimating the total volume of sediment transported in suspension. In this paper, suspended sediment concentration profiles were not extrapolated to the free-surface so as to avoid introducing additional error.

The net volume of sediment transported as sheet flow (magnitude and direction) is directly related to the approximated velocity profiles in the sheet layer (Figure 5). The sensitivity of the net transported volume in the sheet layer as a function of the profile shape parameter, α, in equation (2) should be evaluated in ongoing research efforts related to the BARSED data. The formula used to approximate velocity profiles in the sheet layer, equation (2), implies that velocities within the sheet layer are exactly in phase with velocities at the top of the sheet layer and maintain a constant profile shape. Both conditions are not likely to occur (e.g. Berni et al., 2013). Improved sensing technology, such as the acoustic concentration and velocity profiler, ACVP (Hurther et al., 2011; Revil-Baudard et al., 2015), as well as ongoing development of multi-phase numerical sediment transport models (Cheng et al., 2017; Kim et al., 2017) may lead to a better understanding of velocities in the sheet flow layer under skewed-asymmetric surface waves in the presence of sediment.

Acknowledgements

This work was funded under NSF grant numbers OCE-1356855, OCE-1356978 and 1314109-DGE. The two FOBS sensors were provided by the U.S. Army Corps of Engineers. The authors thank Pedro Lomonaco, Tim Maddux and Cooper Pearson at the O.H. Hinsdale Wave Research Laboratory for their contribution to this project. The authors would like to thank the following researchers/visitors for their help during the experiment: P. Chardón-Maldonado, Y. Kim, D. Krafft, J. Pintado-Patiño, W. Pringle, T. Suzuki, Y. Wang, and Z. Zhou.

References

Anderson, D., Cox, D.T., Mieras, R.S., Puleo, J.A., and Hsu, T., In Review. Observations of wave-induced pore pressure gradients and bed level response on a surf zone sandbar. *J. Geophys. Res. Oceans.*

Bagnold, R.A., 1956. The flow of cohesionless grains in fluids. Proc. *Roy. Soc. Lond. A*, *Math. Phys. Sci.*, 249(964): 235-297.

Bailard, J.A., 1981. An energetics total load sediment transport model for a plane sloping beach. *J. Geophys. Res.*, 86(C11): 10938–10954.

Beach, R.A., Sternberg, R.W. and Johnson, R., 1992. A fiber optic sensor for monitoring suspended sediment. *Marine Geology*, 103(1): 513–520.

Berni, C., Barthélemy, E. and Michallet, H., 2013. Surf zone cross-shore boundary layer velocity asymmetry and skewness: An experimental study on a mobile bed. *J. Geophys. Res. Oceans*, 118(4): 2188–2200.

Cheng, Z., Hsu, T.-J. and Calantoni, J., 2017. SedFoam: A multi-dimensional Eulerian two-phase model for sediment transport and its application to momentary bed failure. *Coastal Engineering*, 119: 32–50.

Craig, R.G.A., Loadman, C., Clement, B., Rusello, P.J. and Siegel, E., 2011. *Characterization and testing of a new bistatic profiling acoustic Doppler velocimeter: The Vectrino-II*. Paper presented at Current, Waves and Turbulence Measurements (CWTM), 2011 IEEE/OES 10th, March 2011.

Dohmen-Janssen, C.M. and Hanes, D.M., 2002. Sheet flow dynamics under monochromatic nonbreaking waves. *J. Geophys. Res.*, 107(C10): 3149.

Fernández-Mora, A., Calvete, D., Falqués, A. and de Swart, H.E., 2015. Onshore sandbar migration in the surf zone: New insights into the wave-induced sediment transport mechanisms. *Geophys. Res. Lett.*, 42(8): 2014GL063004.

Gallagher, E.L., Elgar, S. and Guza, R.T., 1998. Observations of sand bar evolution on a natural beach. *J. Geophys. Res.*,

103(C2): 3203–3215.
Hoefel, F. and Elgar, S., 2003. Wave-Induced Sediment Transport and Sandbar Migration. *Science*, 299(5614): 1885–1887.
Hurther, D., Thorne, P.D., Bricault, M., Lemmin, U. and Barnoud, J.-M., 2011. A multi-frequency Acoustic Concentration and Velocity Profiler (ACVP) for boundary layer measurements of fine-scale flow and sediment transport processes. *Coastal Engineering*, 58(7): 594–605.
Kim, Y., Cheng, Z., Hsu, T., Mieras, R.S., and Puleo, J.A., 2017. A numerical investigation of sheet flow under non-breaking and breaking waves. Proc. of the *8th International Conference on Coastal Dynamics*, June 12-16, Helsingør, Denmark.
Lanckriet, T., Puleo, J., Masselink, G., Turner, I., Conley, D., Blenkinsopp, C. and Russell, P., 2014. Comprehensive Field Study of Swash-Zone Processes. II: Sheet Flow Sediment Concentrations during Quasi-Steady Backwash. *Journal of Waterway, Port, Coastal, and Ocean Engineering*, 140(1): 29–42.
Lanckriet, T., Puleo, J.A. and Waite, N., 2013. A Conductivity Concentration Profiler for Sheet Flow Sediment Transport. *IEEE Journal of Oceanic Engineering*, 38(1): 55–70.
Mieras, R.S., Puleo, J.A., Anderson, D., Cox, D.T., and Hsu, T., In Review. Large-scale experimental observations of sheet flow on a sandbar under skewed-asymmetric waves, *J. Geophys. Res. Oceans*.
Nielsen, P., 1992. *Coastal Bottom Boundary Layers and Sediment Transport*. World Scientific.
O'Donoghue, T. and Wright, S., 2004. Concentrations in oscillatory sheet flow for well sorted and graded sands. *Coastal Engineering*, 50(3): 117–138.
Plant, N.G., Holland, K.T., Puleo, J.A. and Gallagher, E.L., 2004. Prediction skill of nearshore profile evolution models. *J. Geophys. Res.*, 109(C1): C01006.
Pugh, F.J. and Wilson, K.C., 1999. Velocity and Concentration Distributions in Sheet Flow above Plane Beds. *Journal of Hydraulic Engineering*, 125(2): 117–125.
Puleo, J.A., Krafft, D.R., Pintado-Patiño, J.C., and Bruder, B., In Revision. Video-derived near bed and sheet flow velocities in dam-break-driven swash. Submitted to *Coast. Eng.*
Revil-Baudard, T., Chauchat, J., Hurther, D. and Barraud, P.-A., 2015. Investigation of sheet-flow processes based on novel acoustic high-resolution velocity and concentration measurements. *Journal of Fluid Mechanics*, 767: 1–30.
Ribberink, J.S., van der Werf, J.J., O'Donoghue, T. and Hassan, W.N.M., 2008. Sand motion induced by oscillatory flows: Sheet flow and vortex ripples. *Journal of Turbulence*, 9: N20.
Ruessink, B.G. and Kuriyama, Y., 2008. Numerical predictability experiments of cross-shore sandbar migration. *Geophys. Res. Lett.*, 35(1): L01603.
Scott, C.P., Cox, D.T., Maddux, T.B. and Long, J.W., 2005. Large-scale laboratory observations of turbulence on a fixed barred beach. *Measurement Science and Technology*, 16(10): 1903.
Sumer, B.M., Kozakiewicz, A., Fredsoe, J. and Deigaard, R., 1996. Velocity and Concentration Profiles in Sheet-Flow Layer of Movable Bed. *Journal of Hydraulic Engineering*, 122(10): 549–558.
Traykovski, P., 2007. Observations of wave orbital scale ripples and a nonequilibrium time-dependent model. *J. Geophys. Res.*, 112(C6): C06026.
Van der Zanden, J., 2016. *Sand Transport Processes in the Surf and Swash Zones*. PhD Thesis, University of Twente, The Netherlands.
Wang, Y.-H. and Yu, G.-H., 2007. Velocity and concentration profiles of particle movement in sheet flows. *Advances in Water Resources*, 30(5): 1355–1359.